

Cluster deprojection combining multiple observable data sets

K. Reblinsky

Max-Planck-Institut für Astrophysik, Postfach 1317, 85741 Garching, Germany (reblinsk@mpa-garching.mpg.de)

Received 8 September 2000 / Accepted 6 October 2000

Abstract. In this paper a general, parameter-free algorithm for the deprojection of observed, two-dimensional cluster images is proposed. The algorithm is based on the Richardson-Lucy algorithm for the rectification of observed distributions, and it combines multiple sets of observable data from clusters of galaxies – weak lensing (lensing potential ψ), X-ray (X-ray surface brightness S_X), and Sunyaev-Zel’dovich (temperature decrement ΔT_{SZ}) images – to obtain information on the structure along the line-of-sight, namely the 3-dim. gravitational potential φ .

For the derivation of this *multiple-data Richardson-Lucy deprojection algorithm* we specify a geometrical model for the cluster assuming axial symmetry only. We demonstrate the quality of the reconstructions using gas-dynamical simulations assuming an inclination angle for the cluster. The achieved deprojections are shown to yield a stable and unique reconstruction of the 3-dim. structure of the cluster. Strategies for determining the inclination angle and the weight factors used for the reconstruction are discussed. In the end we provide an outlook on the suitability of the algorithm for practical applications to true observational data.

Key words: galaxies: clusters: general – cosmology: gravitational lensing – cosmology: observations – cosmology: dark matter

1. Introduction

The question of how to deproject observed cluster images is a prime example for so-called *inverse problems*, which often arise in astronomy. As pointed out by Lucy (1974, 1994) inverse problems in astronomical research reflect the fact that it is in general not possible to directly measure the quantities of interest due to the large distances between observers and studied objects. Furthermore, the theoretical understanding of the relevant physical phenomena is often so limited or the problem is so complex, that it is not possible to derive appropriate models from first principles.

At the same time the 3-dim. structure of rich galaxy images is particularly interesting as it impacts on the physical and cosmological interpretation of clusters of galaxies in general.

The shape of a cluster is relevant for the combined analysis of Sunyaev-Zel’dovich (SZ), X-ray, and lensing data, e.g. when the Hubble constant H_0 is determined from SZ-and X-ray images (Gunn 1978; Silk & White 1978; Cavaliere et al. 1979; see Sulkanen 1999 for a first estimation of systematic errors introduced by galaxy cluster shapes) a galaxy cluster shape has to be assumed. The same is true for different cluster mass determinations as projection effects are, at least partly, suspected to account for the discrepancy of the different mass determinations from lensing, X-ray or dynamical mass estimates (Bartelmann & Steinmetz 1996). In addition, it is important for understanding the cluster galaxy orbit structure (The & White 1986; Merritt 1987) and also the baryon mass fraction (White & Frenk 1991; Böhringer et al. 1993).

Here we employ for the deprojection of clusters of galaxies an extension of the classical algorithm of Richardson (1972) and Lucy (1974). It has widely been used for the rectification of optical images. In addition, it has been applied to determine the 3-dim. stellar orbit structure in elliptical galaxies (e.g. Binney et al. 1990; Dehnen & Gerhard 1993, 1994). In order to optimize the results of the reconstruction we combine different data sets, in this case the lensing potential ψ , the X-ray surface brightness S_X and the Sunyaev-Zel’dovich effect. For more and more clusters these high quality data sets become available. The combination of multiple data sets allows one to exploit the different dependences of the various observable distributions on the gravitational potential along the line-of-sight (LOS hereafter).

The plan of the paper is as follows: For deriving this *multiple-data Richardson-Lucy deprojection algorithm* we first describe the general Richardson-Lucy (hereafter RL) approach in Sect. 2, then we specify a geometrical model for the cluster that is suitable for deriving a RL-type deprojection equation for the gravitational potential φ ; in Sect. 3 we discuss the dependencies of the three considered observable distributions, namely the lensing potential, the X-ray emissivity and the Sunyaev-Zel’dovich effect, on the gravitational potential. Finally, in Sect. 4 we show how the three above-mentioned observable distributions can be incorporated into this deprojection procedure. We also discuss strategies for implementing the algorithm into computer programs, and study their respective numerical stability. In Sect. 5 we assess the performance of the algorithm by applying it to synthetic cluster data from

gas-dynamical simulations. In Sect. 6 we briefly show how the inclination angle can be recovered from the data using a χ^2 minimization. In the end, we give an outlook on the suitability of the algorithm for practical applications to true observational data.

2. Formalism

In this section we briefly review the classical Richardson-Lucy algorithm and its features in order to provide a basic understanding of the multiple-data Richardson-Lucy algorithm.

2.1. Richardson-Lucy algorithm

The projection of observables along the LOS can be formulated as an inverse problem, mathematically such problems can be cast into the form of a Fredholm integral equation of the first kind,

$$\psi(x) = \int \phi(\zeta)P(x|\zeta) d\zeta, \quad (1)$$

where $\phi(\zeta)$ is the function of interest, $\psi(x)$ is the function accessible through observation, and the integral kernel $P(x|\zeta)$ reflects the measurement process. In general, ϕ and ψ represent probability density functions, which implies that they and the kernel $P(x|\zeta)$ obey normalization and non-negativity constraints. $P(x|\zeta)dx$ is the probability – presumed to be known – that x' will fall in the interval $(x, x + dx)$ when it is known that $\zeta' = \zeta$.

Richardson (1972) and Lucy (1974, 1994) recognized that the problem is statistical in nature and proposed an iterative inversion algorithm, consisting of the following two steps:

$$\psi_n(x) = \int \phi_n(\zeta)P(x|\zeta)d\zeta, \quad (2a)$$

$$\phi_{n+1}(\zeta) = \phi_n(\zeta) \int \frac{\tilde{\psi}(x)}{\psi_n(x)} P(x|\zeta) dx, \quad (2b)$$

where the ψ denotes the observed distribution, while $\tilde{\psi}$ is the measured quantity having sampling errors. A derivation of the iterative algorithm based on *Bayes' theorem* for conditional probabilities can be found in Lucy (1974).

The iteratively constructed functions ϕ_n satisfy the non-negativity constraint: From Eq. (2b) it follows that $\phi_n \geq 0$ if $\phi_0 \geq 0$. The normalization constraint is fulfilled, as one can prove by integrating Eq. (2b) with respect to ζ and using the normalizations of the probabilities $Q_n(\zeta|x)d\zeta$ and $\tilde{\psi}_n dx$.

Ideally we would like an iterative algorithm to converge to the exact solution, and from Eq. 2 it can be seen that the above scheme converges if $\psi_n(x)$ is sufficiently close to $\tilde{\psi}(x)$ for all points x , except for those in a set of zero measure. However, this inherent convergence criterion is much too strong for practical purposes where $\tilde{\psi}(x)$ may be contaminated by non-negligible measurement errors. Looking again at the two coupled Eqs. 2a and 2b, we see that deviations of $\tilde{\psi}/\psi_n$ from unity on a length

scale large compared to that of $P(x|\zeta)$ are removed in essentially one iteration, whereas deviations on a small length scale are mostly averaged out when convolved with $P(x|\zeta)$, and result only in small corrections to ϕ_n . Thus the algorithm has the property of first fitting the large-scale differences between the given initial guess and the true solution, while it fits the small-scale fluctuations only in later iteration steps. Under the reasonable assumption that the small scale fluctuations are more likely to be caused by statistical errors in $\tilde{\psi}$, this behaviour of the RL algorithm is indeed highly desirable. It ensures that the RL procedure very quickly results in an approximate solution in which most of the significant information in the observed $\tilde{\psi}$ is already recovered. But one has to keep in mind that there is *no obvious* convergence criterion for recovering the large-scale fluctuations only; in general it is not easy to say when one starts to fit small-scale statistical fluctuations. Thus, for the algorithm to work, one has to know and to control the errors in the measured data very well.

2.2. Richardson-Lucy algorithm: the axisymmetric case

After deriving the basic RL-algorithm and discussing its features, we need to specify a cluster model in order to derive the kernel $P(x|\zeta)$ and formulate the RL-scheme for this specific model.

Consider a cluster of galaxies covered by a system of cartesian coordinates (X, Y, Z) . We are interested in recovering the distribution of some physical quantity $\phi(X, Y, Z)$, which we assume to have axial symmetry with respect to the Z -axis of the cluster coordinate system:

$$\phi(X, Y, Z) \equiv \phi(R, Z) \quad \text{with} \quad R^2 = X^2 + Y^2. \quad (3)$$

Furthermore, we assume that the projection of ϕ is observed as some quantity ψ , where the observer's coordinate system (x, y, z) is inclined by an angle i , and in which $x = X$ and z is the LOS (see Fig. 1). The transformation between cluster coordinates (X, Y, Z) and observer's coordinates (x, y, z) is thus given by

$$X = x, \quad (4a)$$

$$Y = y \cos(i) - z \sin(i), \quad (4b)$$

$$Z = y \sin(i) + z \cos(i), \quad (4c)$$

and the observed projection ψ is given as the LOS integral over ϕ ,

$$\psi(x, y) = \int dz \phi(R(x, y, z), Z(x, y, z)). \quad (5)$$

If we want to apply the RL-algorithm to recover ϕ from ψ , we first have to bring the fundamental LOS integral 5 into the form of Eq. 1,

$$\psi(x, y) = \int dR \int dZ P(x, y|R, Z)\phi(R, Z), \quad (6)$$

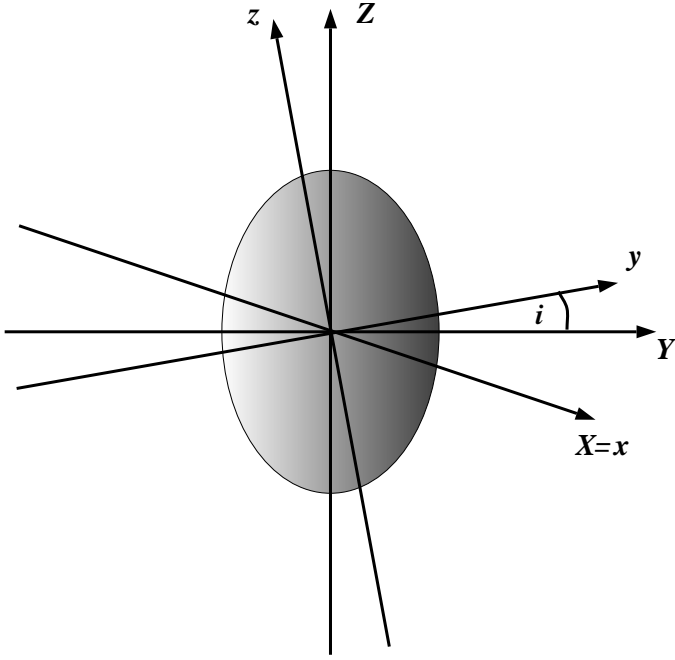


Fig. 1. Display of the relation between cluster coordinates (X, Y, Z) and observer's coordinates (x, y, z) assuming axial symmetry.

where $P(x, y|R, Z)$ has to be normalized to unity. The derivation follows closely the derivation for elliptical galaxies given in Binney et al. (1990) and is reproduced in Appendix A. We can identify the kernel

$$P(x, y|R, Z) = \frac{\delta[(\frac{y}{\cos i} - Z \tan i)^2 - (R^2 - x^2)]}{\pi \cos i}, \quad (7)$$

and find that it is properly normalized:

$$\int_{-\infty}^{\infty} dx \int_{-\infty}^{\infty} dy P(x, y|R, Z) = 1. \quad (8)$$

Having the explicit expression 7 for the kernel $P(x, y|R, Z)$, we could now start to apply the RL-scheme for recovering $\phi(R, Z)$ from an observed $\psi(x, y)$ by means of Eqs. (2.1 a,b). However, since the probability kernel $P(x, y|R, Z)$ contains a δ -function, which is notoriously difficult to deal with in the context of discretized grid-data, we have chosen to reformulate the main Eqs. (2.1 a,b) for this special axisymmetric case.

For the first integral of the iterative scheme the formulation A.5 of the integral using the probability kernel $P(x, y|R, Z)$ is not necessary. Instead, this integral can be evaluated as a simple integral along the LOS,

$$\psi_n(x, y) = \int_{-\infty}^{\infty} dz \phi_n(R(x, y, z), Z(x, y, z)), \quad (9)$$

where the coordinate transformation (4c) is used to evaluate the integration along z . The integral (9) is analytically equivalent to the integral A.5, but not numerically. The approach using the probability kernel $P(x, y|R, Z)$ as in the integral (2a), which was used in Binney et al. (1990), involves the δ -functions. For our purpose, we found the approach given in A.5 to be numerically extremely unstable, and therefore we employed the direct approach stated in (9).

The second step 2b in the iterative RL-scheme reads in our case

$$\frac{\phi_{n+1}(R, Z)}{\phi_n(R, Z)} = \int dx \int dy \frac{\tilde{\psi}(x, y)}{\psi_n(x, y)} P(x, y|R, Z). \quad (10)$$

For this second integral the evaluation of the probability kernel $P(x, y|R, Z)$ cannot be avoided. However, it is possible to eliminate the δ -function by again applying the same rule as reproduced in the Appendix to $\delta(f(y))$ and by subsequently integrating over y as is again demonstrated in Appendix A. The calculation leads to our final result, namely a formulation for the second integral in the RL-scheme without δ -functions:

$$\frac{\phi_{n+1}(R, Z)}{\phi_n(R, Z)} = \frac{1}{2\pi} \sum_{\pm} \int_{-\pi}^0 dt \frac{\tilde{\psi}(R \cos t, Z \sin i \pm R \sin t \cos i)}{\psi(R \cos t, Z \sin i \pm R \sin t \cos i)}. \quad (11)$$

Please note that the integral (11) describes a full ellipse on the sky. The difference between Eq. (11) and the Appendix of Binney et al. (1990) is, that Eq. (11) uses the full information on the ellipse, while Binney et al. (1990), use only half of it. This formulation has the advantage that no assumptions on the data are made, i.e. the latter are not assumed to be symmetric along any of the projection axes.

3. Observables sensitive to the LOS-structure

As already stated in the introduction, the overall goal is to combine multiple data sets within the Richardson-Lucy algorithm to deproject cluster images. For observed distributions – denoted as ψ in the previous sections – we now discuss concrete observables, namely the weak lensing potential, the X-ray surface brightness and the SZ temperature decrement. For employing the Richardson-Lucy algorithm, it is important to connect the observables to the theoretical distribution ϕ . We choose the gravitational potential φ as theoretical distribution. In principle it is possible to choose the density ρ as theoretical distribution, but the gravitational potential φ possesses better symmetry properties than the density ρ . Therefore substructure has less impact on the potential than on the density, thus better fulfilling the symmetry assumptions made deriving the kernel $P(x, y|R, Z)$.

In the following we briefly discuss the connection between the respective observable and the gravitational potential φ needed for the derivation and implementation of the MDRL-algorithm.

3.1. Lensing potential

Weak gravitational lensing emerged in the past couple of years as a tool to map the mass distribution of clusters of galaxies (e.g. Clowe et al. 2000 for one recent example). For a derivation and discussion of gravitational lensing theory cf. Schneider et al. (1992). Here we concentrate on the effective lensing potential

ψ , which can be written as the appropriately scaled, projected Newtonian potential of the lens

$$\psi(x, y) = \frac{D_{\text{ds}}}{D_{\text{d}}D_{\text{s}}} \frac{2}{c^2} \int \varphi(D_{\text{d}}x, D_{\text{d}}y, z) dz. \quad (12)$$

D_{s} , D_{d} , and D_{ds} are the angular-diameter distances from the observer to the sources, from the observer to the lens, and from the lens to the sources. The scaled lensing potential ψ can be directly obtained from the observed data using a maximum likelihood approach (Bartelmann et al. 1996). The lensing potential is connected to the local properties of the lens, namely the convergence κ , and the shear $\gamma = \gamma_1 + \gamma_2$ in terms of the second derivatives of $\psi(x, y)$

$$\kappa(x, y) = \frac{1}{2} \nabla^2 \psi(x, y), \quad (13a)$$

$$\gamma_1(x, y) = -\frac{1}{2} (\psi_{,11} - \psi_{,22}), \quad (13b)$$

$$\gamma_2(x, y) = -\psi_{,12}, \quad (13c)$$

where indices i following commas denote partial derivatives with respect to x_i .¹

Hereafter, ψ shall exclusively denote the lensing potential. In Eq. 12 the dependence of the lensing potential on the 3-dim. gravitational potential φ is given as the LOS integral

$$\psi(x, y) \propto \int_{-\infty}^{\infty} \varphi(R, Z) dz. \quad (14)$$

With current observational techniques the lensing potential of clusters can be determined up to a radius of ≤ 1.5 Mpc from the center.

3.2. X-ray emissivity

Clusters of galaxies are powerful X-ray emitters with luminosities in the range of (10^{43} – 10^{45}) erg s⁻¹, making them the most luminous X-ray emitters in the sky. The X-ray emission in clusters is extended rather than point-like, and the X-ray spectra are best explained by thermal *bremsstrahlung* (free-free radiation) from the hot, dilute plasma with temperatures in the range (10^7 – 10^8) K and densities of $\approx 10^{-4}$ – 10^{-3} particles per cm³.

For the present purpose it is sufficient to include continuum emission only. Semiclassical derivations of free-free emission can be found in standard textbooks, e.g. in Rybicki & Lightman (1979) and in Shu (1991). The emissivity at a frequency ν associated with electrons accelerated by ions of charge Z_e in a plasma with temperature T is given by

$$j_{\nu} = \frac{2^5 \pi e^6}{3 m_e c^3} \left(\frac{2\pi}{3 m_e k} \right)^{1/2} \times Z^2 n_e n_i g_{\text{ff}}(Z, T, \nu) T^{-1/2} \exp\left(-\frac{h\nu}{kT}\right), \quad (15)$$

where n_i and n_e are the number densities of ions and electrons, respectively. The Gaunt factor $g_{\text{ff}}(Z, T, \nu)$ corrects for quantum-mechanical effects and for the effect of distant collisions. It is a slowly varying function of frequency and temperature, and can be set to unity for nearly all frequencies and temperatures of practical interest. For a completely ionized gas mixture with a mass ratio of 75% hydrogen and 25% helium, i.e. a gas with a mean mass per particle $\bar{m} = 10^{-24}$ g, the thermal bremsstrahlung at position \mathbf{x} in the energy range $E_a \leq E \leq E_b$ is

$$j_{\mathbf{x}}(\mathbf{x}; E_a, E_b) = 5.53 \times 10^{-24} \text{ erg cm}^{-3} \text{ s}^{-1} \times \left(\frac{kT}{\text{keV}} \right)^{1/2} \left(\frac{n_e}{\text{cm}^{-3}} \right)^2 \left[\exp\left(-\frac{E_a}{kT}\right) - \exp\left(-\frac{E_b}{kT}\right) \right], \quad (16)$$

where the electron density n_e in this case is given by

$$n_e = 0.52 \frac{\rho_{\text{gas}}}{\bar{m}}. \quad (17)$$

The observable X-ray surface brightness received at the 2-dim. position \mathbf{zeta} is the LOS integral of the X-ray emissivity $j_{\mathbf{x}}$,

$$S_{\mathbf{x}}(\zeta; E_a, E_b) = \frac{1}{4\pi(1+z)^3} \int j_{\mathbf{x}}(R, Z; E_a, E_b) dl, \quad (18)$$

where the factor $(1+z)^3$ accounts for the redshifting of the ratio between luminosity distance and angular diameter distance.

Assuming a hydrostatic gas distribution, it is possible to relate the observed X-ray surface brightness $S_{\mathbf{x}}$ to the 3-dim. gravitational potential φ by the Euler equation

$$\nabla P = -\rho_{\text{gas}} \nabla \varphi(R, Z), \quad (19)$$

where the gas pressure P obeys the ideal equation of state

$$P = P_0 \frac{\rho_{\text{gas}}}{\rho_{\text{gas},0}}. \quad (20)$$

For this isothermal gas distribution, where the temperature T is independent of the position we obtain a dependence on the potential φ of the form

$$\rho_{\text{gas}}(R, Z) = \rho_{\text{gas},0} \times \exp\left[-\frac{\bar{m}}{kT} (\varphi(R, Z) - \varphi_0)\right]. \quad (21)$$

We thus arrive at the following relationship between observed X-ray surface brightness $S_{\mathbf{x}}(x, y)$ and the 3-dim. gravitational potential $\varphi(R, Z)$:

$$S_{\mathbf{x}}(x, y) \propto \int_{-\infty}^{\infty} \exp\left[-2\varphi'(R, Z)\right] dz. \quad (22)$$

3.3. Sunyaev-Zel'dovich effect

The inverse Compton scattering of the cosmic microwave background (CMB) radiation field off thermal electrons in clusters of galaxies on, which is called the Sunyaev-Zel'dovich effect (Sunyaev & Zel'dovich 1972, 1978, 1980), is one of the most important astrophysical processes in a low-energy environment, where only small energy transfers occur, with observable consequences. In essence, the Sunyaev-Zel'dovich (hereafter SZ)

¹ Notice the sign of the shear components: We follow the sign convention of Schneider & Seitz (1995).

effect causes a perturbation of the spectrum of the CMB as its photons pass through the hot gas of clusters of galaxies. The SZ-effect is a very important cosmological probe, which can be used to study the evolution and structure of the Universe.

The frequency shift leads to an apparent deficit in intensity at low frequencies of the CMB spectrum, and an increase at higher frequencies meaning that the temperature of the CMB photons is lowered through the SZ-effect. Here we assume that the temperature decrement ΔT_{SZ} at certain frequencies can be measured. The temperature decrement as a function of redshift, expressed in terms of the Rayleigh-Jeans brightness temperature ($T_{\text{RJ}} = (\lambda^2/2k)I$), is given as

$$\Delta T_{\text{SZ}} = \left(\frac{x}{e^x - 1} \right)^2 e^x \left(x \coth \frac{x}{2} - 4 \right) y T_{\text{CMB}}, \quad (23)$$

where y is the Comptonization parameter

$$y = \int \left(\frac{kT_e}{m_e c^2} \right) (\sigma_T n_e) dl, \quad (24)$$

and $x = h\nu/kT_{\text{CMB}}$. The first term of the comptonization parameter y describes the effect on energy transfer by a single electron, while the second term gives the probability. As opposed to the X-ray case which depends on $n_e^2 T^{1/2}$, the SZ-effect depends on $n_e T \propto \rho T$, which is proportional to the pressure P , thus providing additional constraints on the cluster. As in the X-ray case a hydrostatic gas distribution is assumed. Therefore the temperature decrement depends on the gravitational potential in the following way

$$\Delta T_{\text{SZ}}(x, y) \propto \int_{-\infty}^{\infty} \exp(-\varphi'(R, Z)) dz. \quad (25)$$

It is worthwhile noting that for both, the X-ray surface brightness S_x and the SZ-temperature decrement ΔT_{SZ} , the dependence on the quantity of interest, the 3-dim. gravitational potential φ , is exponential, requiring great care in the numerical implementation.

4. Multiple-data Richardson-Lucy deprojection

Now we propose the multiple-data Richardson-Lucy deprojection (MDRL) algorithm. The combination of different data sets can be achieved in three separate steps. The first step of the algorithm is to compute the three LOS integrals

$$\psi_n(x, y) \propto \int_{-\infty}^{\infty} dz \varphi_n(\mathbf{R}(x, y, z), \mathbf{Z}(x, y, z)), \quad (26a)$$

$$S_{x,n}(x, y) \propto \int_{-\infty}^{\infty} dz \times \exp(-2\varphi_n(\mathbf{R}(x, y, z), \mathbf{Z}(x, y, z))), \quad (26b)$$

$$\Delta T_{\text{SZ},n}(x, y) \propto \int_{-\infty}^{\infty} dz \times \exp(-\varphi_n(\mathbf{R}(x, y, z), \mathbf{Z}(x, y, z))), \quad (26c)$$

resulting in iterated input data ψ_n , $S_{x,n}$, and ΔT_{SZ} . In the second step we define the three integrals

$$F_n(R, Z) = \int f_n(x, y) P(x, y|R, Z) dx dy, \quad (27a)$$

$$G_n(R, Z) = \int g_n(x, y) P(x, y|R, Z) dx dy, \quad (27b)$$

$$H_n(R, Z) = \int h_n(x, y) P(x, y|R, Z) dx dy, \quad (27c)$$

where f_n , g_n and h_n are defined as

$$f_n = \frac{\tilde{\psi}}{\psi_n} \quad ; \quad g_n = \frac{\tilde{S}_x}{S_{x,n}} \quad ; \quad h_n = \frac{\tilde{\Delta T}_{\text{SZ}}}{\Delta T_{\text{SZ},n}}. \quad (28)$$

Here $\tilde{\psi}$, \tilde{S}_x , and $\tilde{\Delta T}_{\text{SZ}}$ denote the observed input distributions.

In the second step above the three integrals – for the lensing potential ψ the integral (27a), for the X-ray surface brightness S_x integral (27b), and for the SZ temperature decrement ΔT_{SZ} the integral (27c) – correspond to the integral (2b) of Richardson-Lucy's iterative inversion algorithm, while the Eqs. (26a) – (26c) correspond to the integral (2a) of the inversion algorithm.

In order for the multiple-data Richardson-Lucy algorithm to work the results of the integrations have to be combined after every iteration step as

$$\varphi_{n+1} = \alpha \varphi_n F_n + \beta \left(\varphi_n - \frac{1}{2} \ln G_n \right) + \gamma \left(\varphi_n - \ln H_n \right). \quad (29)$$

α , β , and γ are weighting factors with $\alpha + \beta + \gamma = 1$, which can be used to determine the relative weight put on the respective input data. By means of these weighting factors, it is possible to recover the case of having just one set of measured data.

As already mentioned in Sect. (3) for the X-ray case and the SZ-case the dependence on the gravitational potential φ is exponential. Thus it is necessary for these two cases to take the logarithm of the integrals (27b) and (27c) in order to reconstruct the gravitational potential. The factor 1/2 for the X-ray integral G_n arises due to the fact that the X-ray surface brightness depends on the electron density n_e^2 and not n_e .

Eq. (29) completes the multiple-data Richardson-Lucy deprojection algorithm, thus constituting the third step. In terms of the iterative inversion algorithm this step corresponds to the evaluation of the full Eq. (2b).

4.1. Implementation of the multiple-data Richardson-Lucy deprojection

The implementation of the program follows closely the formulation of the MDRL-algorithm given in the last section. For the algorithm, two different types of integrals need to be evaluated. After reading the observed data and assuming an initial guess for the gravitational potential the iteration cycle is entered. The first step in the iteration cycle is to integrate the gravitational potential φ according to Eqs. (26a) – (26c), to obtain the iterated ψ_n , $S_{x,n}$, and $\Delta T_{\text{SZ},n}$. Now the results of this *first* integration can be used to compute the integrals (27a) – (27c) that constitute the *second* integration. The last step of the iteration cycle is to compute the new estimate for the gravitational potential φ_{n+1} from Eq. (29). This new, improved estimate of the gravitational

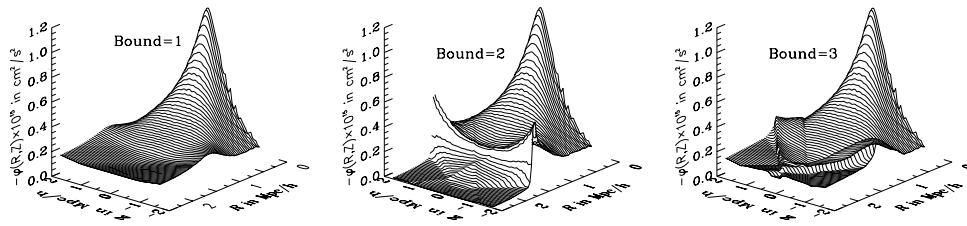


Fig. 2. Gravitational potential of a cluster from a gas-dynamical simulation reconstructed from lensing data using different boundary conditions in the second integration of the axisymmetric RL algorithm. The enumeration of the boundary conditions is as in Sect. 4.1.

potential is used to reenter the iteration cycle. The whole algorithm is stopped after a few iterations; usually 7–8 iterations lead to satisfactory results for the potential when compared to the original potential as obtained from cluster simulations.

Both, the input data ψ_0 , $S_{x,0}$, $\Delta T_{SZ,0}$ and the gravitational potential φ are represented as discretized data on a rectangular grid. The observed data is assumed to cover a *finite* data field $(x_{\min}, x_{\max}) \times (y_{\min}, y_{\max})$, and the reconstructed potential thus covers a corresponding field $(R_{\min}, R_{\max}) \times (Z_{\min}, Z_{\max})$, in cluster coordinates (R, Z) .

For the first integrals of the iterative scheme (26a)–(26c) we implemented a standard LOS integral in the formulation of Eq. (9). As expected, preliminary tests with the equivalent formulation A.5 via the integral kernel $P(x, y|R, Z)$ as in Binney et al. (1990), did not lead to satisfactory results.

We evaluate the LOS integral by first rotating the discretized gravitational potential before computing an integral along the z -axis.

The second integration (27a)–(27c) yielding F_n , G_n , and H_n is performed on an ellipse as in formula A.15, that was derived for the axisymmetric case in Sec 2.2. For easier reference we explicitly write down the corresponding integral for the lensing case:

$$F_n(R, Z) = \frac{1}{2\pi} \sum_{\pm} \int_{-\pi}^0 dt \frac{\tilde{\psi}(R \cos t, Z \sin i \pm R \sin t \cos i)}{\psi(R \cos t, Z \sin i \pm R \sin t \cos i)}. \quad (30)$$

From Eq. 30 we see that for every given point in the (R, Z) plane the fraction $\tilde{\psi}/\psi$ has to be integrated over an ellipse

$$\begin{pmatrix} x(t) \\ y(t) \end{pmatrix} = \begin{pmatrix} R \cos t \\ Z \sin i \pm R \cos i \sin t \end{pmatrix} \quad t \in [0, 2\pi] \quad (31)$$

that is shifted along the y axis by $Z \sin i$ and contracted in the y -direction by a factor of $\cos i$. Due to the finite range of values for x and y we are faced with the problem that some parts of the ellipse, and thus of our integration path, may not be covered by the input data. This is most likely the case if *both* R and $|Z|$ take medium to large values. Even worse, if *either* R or Z becomes very large, then the full ellipse will be outside the input range for x and y .

Therefore one either has to exclude all ellipses with such large (R, Z) -coordinates or one has to define appropriate “boundary” conditions, i.e. values for the ratio $\tilde{\psi}/\psi_n$, $\tilde{S}_x/S_{x,n}$ and $\tilde{\Delta T}_{SZ}/\Delta T_{SZ,n}$ have to be specified for points (x, y) outside of the data field $(x_{\min}, x_{\max}) \times (y_{\min}, y_{\max})$. We tested in some detail the following three possible choices:

1. Assume a smooth expansion of the values of the ratio *observed / iterated* data sets, e.g. for $x \geq x_{\max}$ and $y \geq y_{\max}$ $F_n(x, y) = F_n(x_{\max}, y_{\max})$, $G_n(x, y) = G_n(x_{\max}, y_{\max})$, and $H_n(x, y) = H_n(x_{\max}, y_{\max})$.
2. Assume a perfect reconstruction, i.e. the ratio *observed / iterated* data sets equals unity: $F_n(x, y) = G_n(x, y) = H_n(x, y) = 1$ for $x \geq x_{\max}$ or $x \leq x_{\min}$ and $y \geq y_{\max}$ or $y \leq y_{\min}$.
3. Assume rotational symmetry for the values of the ratios. This can be achieved by computing the distance to the center of the data field and averaging over all values for the corresponding circle which are inside the data field. However this method is computationally relatively expensive, and the results obtained are poor.

Experimenting with these three different boundary conditions and various sizes of the input field, we found that this boundary problem has no significant influence on the quality of the reconstruction achieved for the central part of the potential. A typical example of this problem is given in Fig. 2, where a lensing based reconstruction of the gravitational potential from a gas-dynamical simulation (see next section) is shown for the three different boundary conditions listed above. It is obvious from Fig. 2 that the conditions No.2 and 3 introduce unphysical numerical artefacts for large values of R that have nothing to do with the true potential. Furthermore, condition No.3 is computationally relatively expensive. Thus we have decided to exclusively use boundary condition number No.1 in the remainder of this chapter.

Taking the logarithm for the X-ray and the SZ-case in Eq. (29), which is due to the exponential dependence in the two cases on the gravitational potential, is numerically a very unstable operation. Small deviations in computing the ratio $\tilde{S}_x/S_{x,n}$ and $\tilde{\Delta T}_{SZ}/\Delta T_{SZ,n}$ are magnified by taking the logarithm, thus preventing convergence of the algorithm. In order to avoid this problem we employed a cut-off criterion for the ratio. This is done at the expense of a slower convergence, but as the algorithm converges very quickly and is computationally inexpensive this does not pose a serious problem.

5. Deprojection of cluster images from gas-dynamical simulations

Having put the multiple-data Richardson-Lucy algorithm together, the next important step is to explore how this algorithm behaves, when it is applied to observed data. In particular, we have to assess the key property of the MDRL algo-

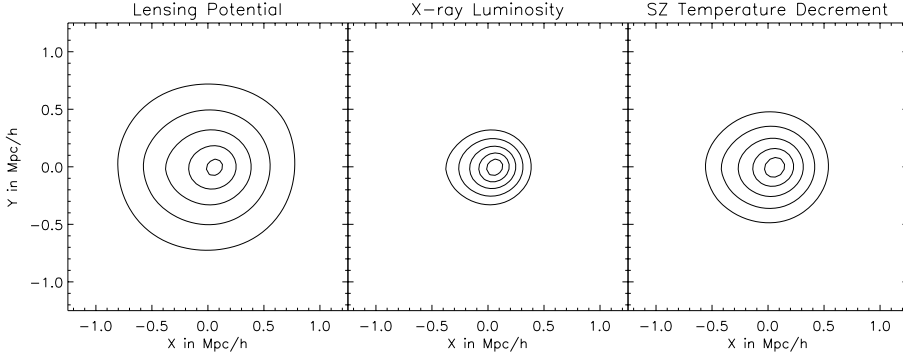


Fig. 3. Input data sets created from the cluster simulation data. Left panel: lensing potential ψ , contours at $(-4, -3.5, -3, -2.5, -2) \times 10^{-8}$. Middle panel: X-ray surface brightness S_x , contours at $(5.75, 5.8, 5.85, 5.9, 5.95) \times 10^{-5}$. Right panel: SZ-temperature decrement ΔT_{SZ} , contours at $(-1.78, -1.77, -1.76, -1.75, -1.74) \times 10^{-2}$.

algorithm, namely the quality of the reconstructed gravitational potential achievable for a given set of input data. Therefore we have to apply the method first to input data for which we know the true gravitational potential. For this purpose we use clusters from gas-dynamical simulations kindly provided by Klaus Dolag (Dolag et al. 1999), to construct observed images for the lensing potential ψ , the X-ray surface brightness S_x , and the SZ-temperature decrement ΔT_{SZ} , reconstruct the gravitational potential φ^{MDRL} , and compare it to the true gravitational potential φ calculated directly from the simulation data. The gas-dynamical simulations include information on the dark-matter distribution, the gas distribution and the temperature of the cluster. They were created using a GRAPE-MSPH code that combines the gravitational interaction of the dark matter component with the hydrodynamics of a gaseous component. In addition, the code includes the magnetohydrodynamic equations following the evolution of the magnetic fields.

The cluster simulations were run using a COBE-normalized CDM power spectrum with a Hubble constant $H_0 = 50 \text{ km s}^{-1} \text{ Mpc}^{-1}$, and $\Omega_0 = 1.0$, $\Omega_\Lambda = 0.0$. The virial mass of the cluster used is $M_{200} \approx 2.4 \times 10^{15} h^{-1} M_\odot$, which resides in a volume of roughly $V \approx (5 h^{-1} \text{ Mpc})^3$. The simulations contain approximately 5×10^4 dark-matter particles and also the same number of gas particles. The dark-matter particles have a mass of $m_{\text{dm}} \approx 1.6 \times 10^{11} h^{-1} M_\odot = 20 \times m_{\text{gas}}$. The masses of the DM and gas particles provide an estimate for the resolution limit of the simulations. For the purpose of mimicking “observed data sets” within current observational limits, the above resolution is completely sufficient.

The gas and DM distributions of single clusters from the simulations are then used to compute the true gravitational potential of the cluster, from which then the observed lensing (Eq. 14), X-ray (Eq. 22), and SZ-data (Eq. 25) are deduced, which in turn serve as input for the MDRL algorithm. Fig. 3 shows three typical input sets created from the gas-dynamical cluster simulation of a single, very massive sample cluster. From the left to the right the lensing potential ψ , the X-ray surface brightness S_x in the energy band 2 keV to 12 keV, and the temperature decrement ΔT_{SZ} at an assumed frequency of 10 GHz are displayed. The inclination angle is fixed at $i = 30^\circ$. If not stated otherwise all reconstructions shown were obtained with 8 iteration steps.

Before turning to the *multiple* data RL-reconstruction of the potential φ , we have to investigate how well the algorithm works

for each of the three different types of input data separately. This means we first consider only the case where φ is deprojected from either lensing, X-ray, or SZ-data alone, and then compare the findings.

We start by looking at different initial guesses for the gravitational potential φ_0 , which are used in the first iteration cycle. Ideally the algorithm should not depend on the choice of the initial guess, therefore two extreme cases for the initial guess are tested and the results are shown in Fig. 4. On the left of Fig. 4 we use a gravitational potential obtained from the universal dark matter profile found by Navarro et al. (1996, 1997; combined NFW) as initial guess, which resembles the original profile rather closely, especially concerning the curvature of the potential. On the right of Fig. 4 we use a plane as initial guess, which makes only minimal assumptions about the potential. Fig. 4 shows the reconstructed gravitational potential φ after 8 iterations for lensing data only, but the results for X-ray and Sunyaev-Zel’dovich data are very similar. Comparing the reconstructed potentials in the lower panels obtained from these completely different initial guesses we clearly see that both initial guesses lead to qualitatively very similar results. The main difference is that the potential reconstructed with the NFW profile as initial guess is steeper in the most central part as opposed to the potential obtained from the plane as initial guess. This can be attributed to the fact that the smallest ellipses with (R, Z) coordinates close to zero are not taken into account for numerical reasons. This is due to the fact that the finite difference formula requires at least four points on the ellipse. Therefore the NFW profile when used as initial guess provides a very high curvature for this part of the potential. In addition, the potential reconstructed from the NFW profile shows less “artefacts” for large (R, Z) -coordinates. Even though the “bump” for large Z -coordinates and R -coordinates is less pronounced for the potential reconstructed from the NFW profile than for the one reconstructed from the plane, the behaviour for these large values of (R, Z) is introduced by the fact that the data field used for the integration is finite. As large (R, Z) -coordinates constitute the boundaries these differences are not relevant for assessing the quality of the reconstruction. For the reconstruction the behaviour in the central $1.5 h^{-1} \text{ Mpc}$ of the cluster is much more important. In this sense the differences found for the two choices of initial guesses are negligible.

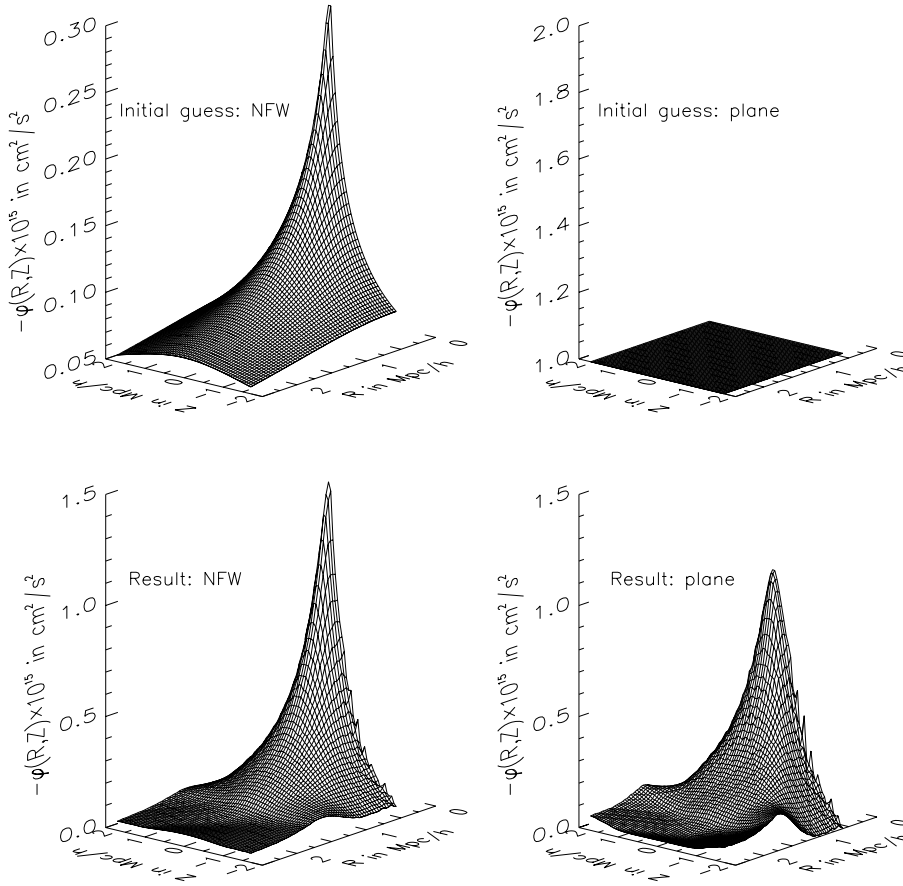


Fig. 4. Comparison of two different initial guesses φ_0 (upper panels) for the reconstruction of the gravitational potential φ . The lower two panels show the reconstructed potential φ^{MDRL} from lensing data after 8 iterations for an inclination angle of $i = 30^\circ$.

The evolution of the reconstructed gravitational potential φ_n with the number of iteration steps n is exemplified in Fig. 5. The potential obtained from the X-ray and SZ case evolves in a qualitatively similar way. The initial guess in this case is a plane shown in the upper left panel, while the lower right panel shows the original potential obtained directly from the simulated cluster. Fig. 5 demonstrates that the algorithm converges extremely fast, even for an initial guess making only minimal a priori assumptions about the cluster potential. Already after the second iteration the potential is in the correct order of magnitude and has acquired the characteristic features of the true cluster potential. In addition, we notice that φ_n is hardly altered in the last two steps, indicating that the algorithm has converged in the sense that most of the large-scale information is recovered. The two main differences between the reconstructed potential from the last step, φ_8 , and the true cluster potential φ is the presence of two “dents” in φ_8 at $(R = 1h^{-1} \text{ Mpc}, Z = \pm 2h^{-1} \text{ Mpc})$, and several small “wiggles” at the flanks of the potential for $R = 0$. We found that the size of the “dents” can be correlated with the finite range of the “observed data”, hinting again at the inherent problems with the finiteness of the boundaries as discussed in Sect. 4.1. The “wiggles” reflecting the property of the algorithm to fit small scale fluctuations last, are in this case probably caused by numerical discretization effects, and thus reflect an unwanted property of the algorithm. This numerical noise can be suppressed by using a smoothing procedure after every iteration step.

In order to gain a better understanding on how the algorithm converges for the three different types of input data, it is instructive to look at the integrals F_n 27a to H_n 27c. For fixed (R, Z) these integrals determine the multiplicative factors that advance φ_n to φ_{n+1} via Eq. 29, and, as already mentioned, good convergence requires that these integrals approach unity. The values of F_n , G_n , and H_n after the last step of Fig. 5 are plotted in Fig. 6. We see that the convergence after 8 iterations is already excellent over the full range of (R, Z) values for all integrals. The X-ray and SZ integrals G_n and H_n both overestimate unity by the same amount and feature a similar shape, reflecting the fact that they have a similar dependence on the potential φ , whereas the lensing integral F_n deviates more strongly from unity to both larger and smaller values, indicating a different convergence behaviour. The main difference is the fact that the integral F_n for small values of R and large values of Z is below unity thus lowering the potential in this range.

We finish the discussion of the reconstruction from single data sources by comparing in Fig. 7 the true, original gravitational potential φ to the results of the reconstructions using the lensing potential, the X-ray surface brightness and the SZ temperature decrement alone as input data for the MDRL algorithm. By this the amount of information on the 3-dim. structure can be determined that is already present in each of the single data sets. Looking at the surface plots of Fig. 7 one sees that all three types of input data give qualitatively very similar results. The lensing reconstruction is superimposed by numerical noise,

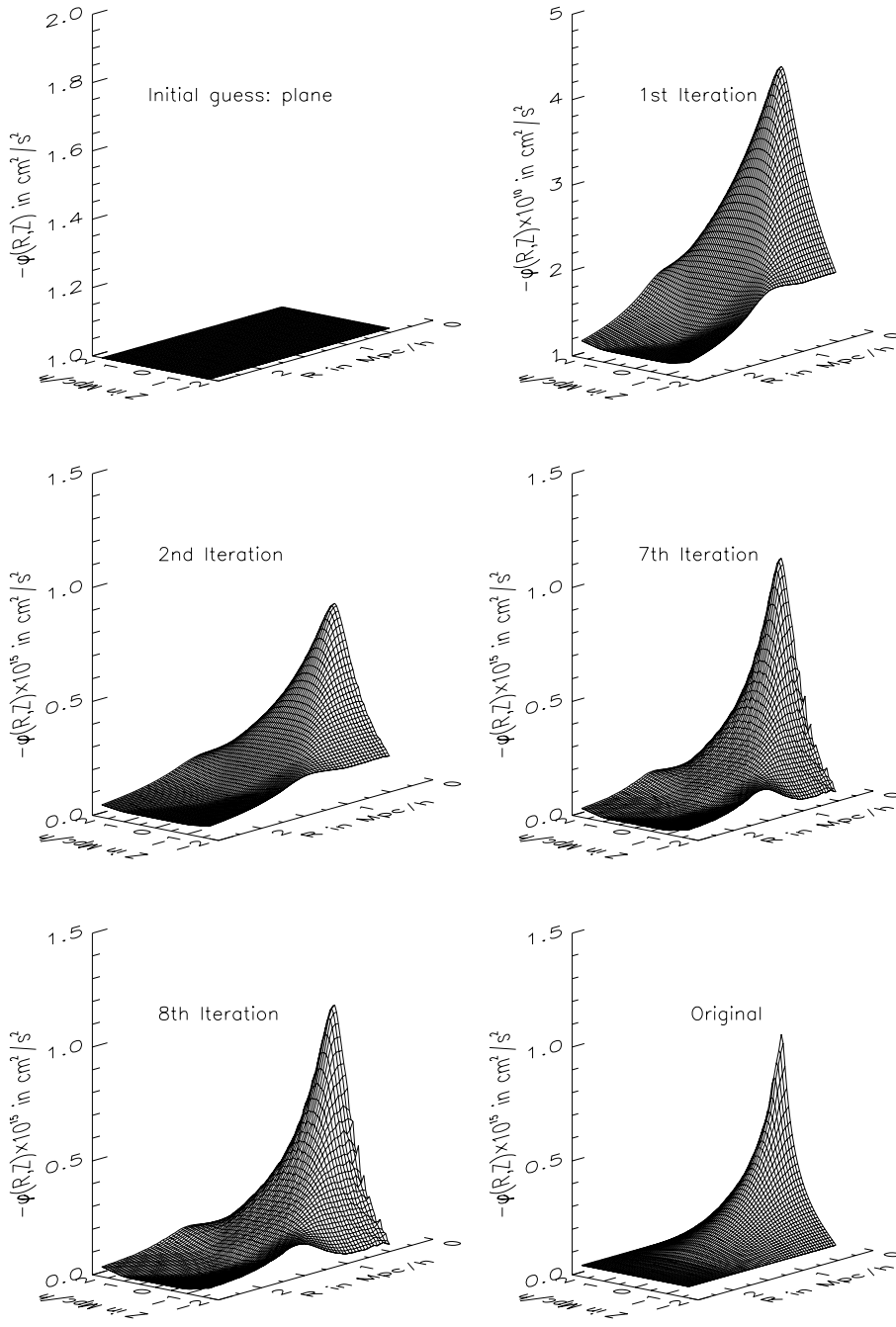


Fig. 5. Display of the iterated gravitational potential φ_n after different iteration steps n . The reconstruction is performed for the lensing potential ψ . The upper left panel shows the initial guess φ_0 , while the lower right panel displays the original cluster potential φ .

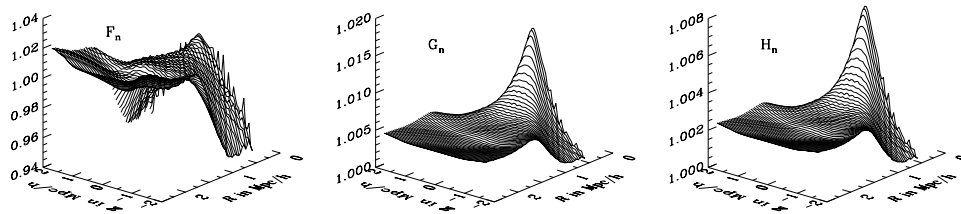


Fig. 6. The integrals F_n (lensing; 27a), G_n (X-ray; 27b), and H_n (SZ; 27c) from the second step of the reconstruction algorithm. The same cluster data as in Fig. 5 was used ($i = 30^\circ$; 8 iterations).

which is also present in the X-ray and SZ case, albeit much less pronounced.

A more detailed comparison of the three reconstructed and the reference potential is possible if surface cuts such as in Fig. 8 are studied. For the cuts through the central part of the cluster

we generally see a good agreement of the three reconstructions with the original potential. The agreement becomes worse for larger radial coordinates as displayed in the right panel of Fig. 8 for the cut through $\varphi(R = 1/2R_{\max}, Z)$. We also notice that the difference between the X-ray and the SZ case is negligible,

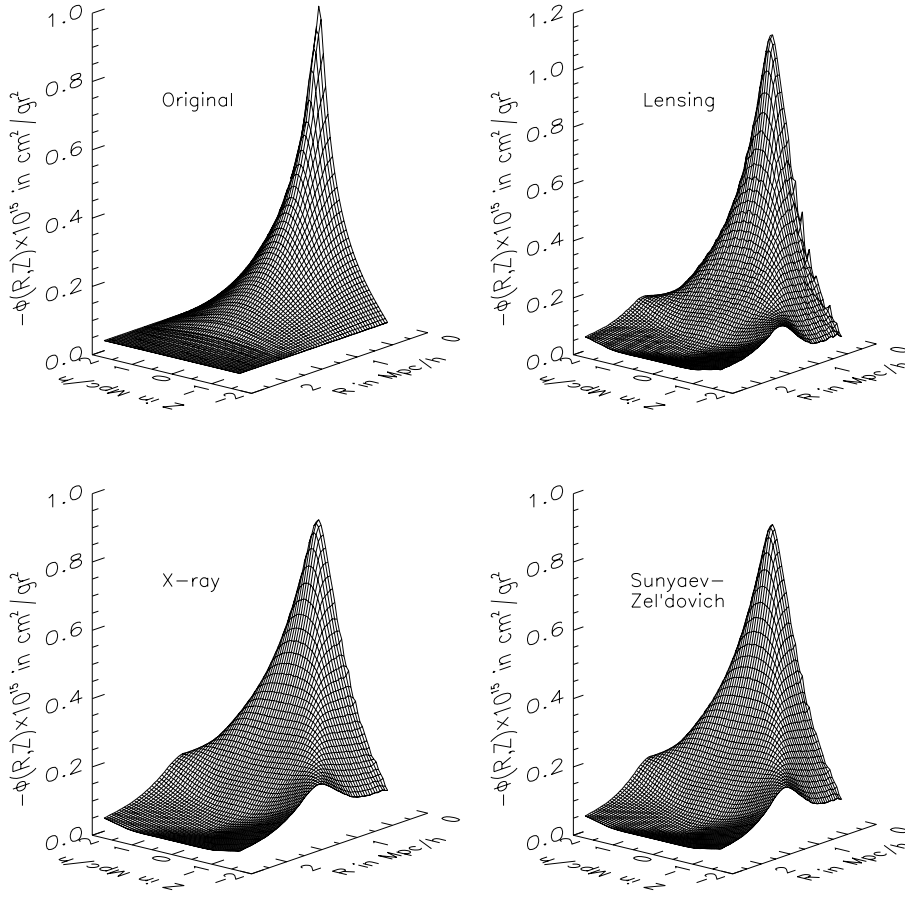


Fig. 7. Comparison of the true, original gravitational potential ϕ (upper left panel) to reconstructions obtained by the lensing potential ψ alone (upper right panel), by the X-ray surface brightness S_x alone (lower left panel), and by the SZ temperature decrement ΔT_{SZ} (lower right panel) alone. The potential is shown in cluster coordinates (R, Z) .

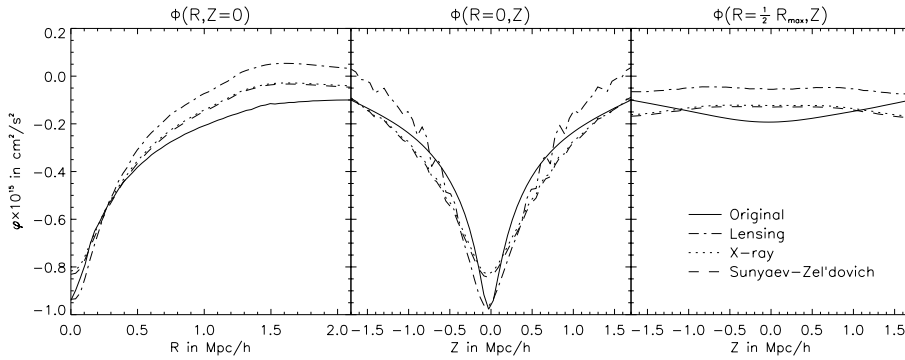


Fig. 8. Comparison of three different cuts through the true, original gravitational potential ϕ and the three single-data reconstructions displayed in Fig. 7.

reflecting their very similar dependence on the gravitational potential.

Compared with the lensing potential ψ both, the X-ray and the SZ data give a very good reconstruction of the inner parts of the potential ($R, |Z| \leq 0.5h^{-1}$ Mpc) which is especially true for the cut along the Z -axis, where the match is nearly perfect. The numerical noise in the lensing potential is more pronounced than in the X-ray and the SZ-case. More importantly, in contrast to the X-ray and SZ-case the curvature and the overall shape of the lensing reconstruction is closer to the true potential even for larger radial coordinates $R \approx 1h^{-1}$ Mpc.

Finally, we are in a position to combine all input data sets for a true *multiple-data reconstruction*, thus allowing a better reconstruction of the gravitational potential ϕ . For the present

example we chose to combine all three data sets with weight factors of 1/3 each. The results of the reconstruction are shown in Fig. 9. In the upper panel we compare two cuts of the result of the reconstruction obtained after 8 iterations with the original potential and the reconstructions computed for the single data sets, respectively. Especially for the cut $\phi(R, Z=0)$ we do see an improvement over the use of just one single data set: The combined reconstruction is more reliable even for values of $R > 1h^{-1}$ Mpc. This leads to better results when compared to the reconstructions obtained from X-ray and SZ data alone. The full surface plots of the original potential and the combined reconstruction demonstrate that the multiple data set reconstruction is able to recover all important features.

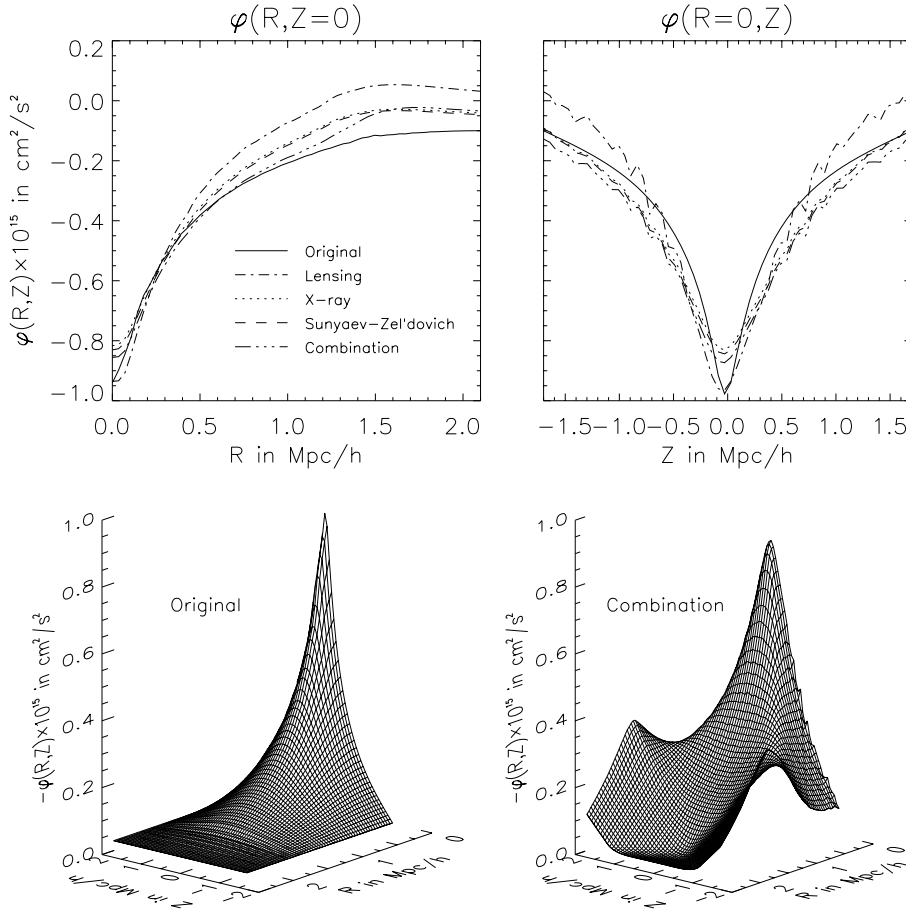


Fig. 9. Result of the reconstruction obtained by combining all data sets shown in Fig. 7, each with a weighting of $1/3$. The upper panel shows two different cuts through the resulting potential comparing the original potential with the results obtained for the combined data set and the results for the single data sets from Fig. 8. The lower panel compares the original potential to the potential reconstructed with the combined data sets as surface plot.

At this point it is worthwhile to assess the quality of the reconstruction in a quantitative way. For this purpose it is instructive to look at the relative errors between the original gravitational potential φ_{orig} and the reconstructed one φ_{rec} , which is computed as $|\varphi_{\text{orig}} - \varphi_{\text{rec}}|/|\varphi_{\text{orig}}|$. In order to compute the relative error we have to shift the potentials in such a way that their respective central parts are on the same level as only the gradient of the potential has a physical meaning. The result for the inner part of the potential, i.e. $R \in (0, 1.0)h^{-1}$ Mpc and $Z \in (-1.0, 1.0)h^{-1}$ Mpc, is displayed in Fig. 10. In the different panels of this figure the relative errors between the original and the reconstructed potential for lensing data (upper left panel), X-ray data (upper right panel), and Sunyaev-Zel'dovich data (lower left panel) are shown; in addition, the result for the combination of all three data types is given in the lower right panel.

For all four reconstructions we see that the deviation over large parts of the potential is less than 5%. When looking at the lensing reconstruction in more detail, we note that in this case the zone with an error margin of less than 5% is relatively wide, especially in the Z -direction. As already noted before, both, the X-ray and the Sunyaev-Zel'dovich reconstruction, show very similar features, which is also reflected in Fig. 10. Both cases give excellent reconstructions in the center with coordinate values (R, Z) of less than $0.5h^{-1}$ Mpc, but the quality of the reconstruction in the outer parts is not as good as in the lensing case. This confirms the theoretical expectation, that the data from X-

ray and SZ measurements, which have their main contributions coming from the cluster core, are less affected by projection effects, nicely complementing the weak lensing data, which is only sensitive to the gravitating matter.

When looking at the results of the combined reconstruction an improvement over the single data reconstructions is obvious. Here the region with error margins of less than 5% is the largest.

Depending on the quality of the data at hand and a priori knowledge of the possibly different levels of noise present in the data, it is possible to adjust the weighting of the different data sets. This is also useful when one is interested in a limited region of the cluster which might be represented more accurately by a certain observable, like e.g. the cluster center which significantly contributes to the X-ray and SZ data. In summary, the combination of data sets can be expected to give improved results, with the astronomer being able to control the reconstruction process by means of the weight factors.

6. χ^2 -based determination of inclination angle i

Clearly in addition to a quantitative assessment of the quality of the reconstruction a systematic procedure for determining the input parameters for the MDRL algorithm is highly desirable.

As explained in Sect. 2.2 the MDRL-algorithm in its current formulation needs to be provided with the inclination angle i as input parameter and a choice for the weight factors α, β

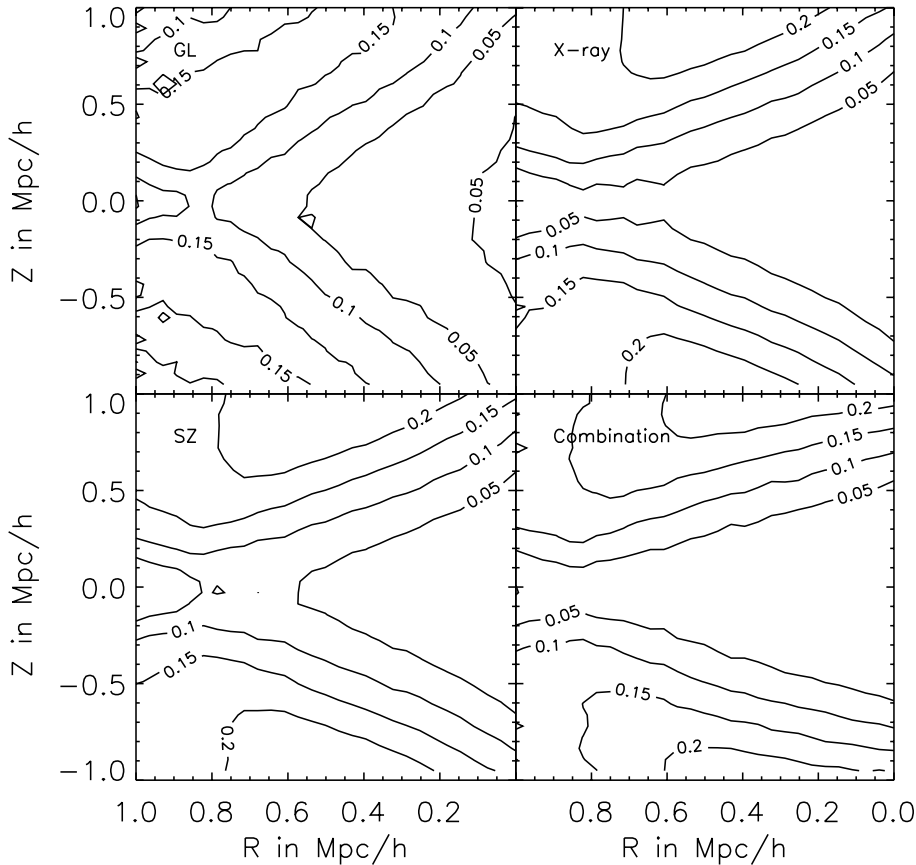


Fig. 10. The relative error between the original gravitational potential $\varphi(R, Z)$ and the reconstructed potential computed as $|\varphi_{\text{orig}} - \varphi_{\text{rec}}|/|\varphi_{\text{orig}}|$. The central part of the potential is displayed: $R \in (0, 1.0)h^{-1}$ Mpc and $Z \in (-1.0, 1.0)h^{-1}$ Mpc. The reconstructions shown are run with the same parameters as in Fig. 8. Upper right panel: lensing data only. Upper left panel: X-ray data only. Lower left panel: Sunyaev-Zel'dovich data only. Lower right panel: Combination of all three data types. Contours mark deviations of (0.05, 0.1, 0.15, 0.2).

and γ for the three different contributions has to be made. Once all these parameters have been specified, the MDRL algorithm yields a reconstructed estimate φ_{rec} for the potential, which in turn determines the best estimates ψ , S_x , and ΔT_{SZ} for the observed input distributions $\tilde{\psi}$ (lensing potential), \tilde{S}_x (X-ray surface brightness), and $\Delta \tilde{T}_{\text{SZ}}$ (Sunyaev-Zel'dovich temperature decrement).

The idea is now to minimize an appropriate χ^2 function, e.g.

$$\chi^2 = \sum_{i=1}^{N_g} \frac{(\tilde{\psi} - \psi(\xi_i))^2}{\sigma_{\text{GL}}^2} + \frac{(\tilde{S}_x - S_x(\xi_i))^2}{\sigma_x^2} + \frac{(\Delta \tilde{T}_{\text{SZ}} - \Delta T_{\text{SZ}}(\xi_i))^2}{\sigma_{\text{SZ}}^2}, \quad (32)$$

to obtain the best parameters within the framework of the model assumptions underlying the presented MDRL algorithm. Here N_g is the number of grid points, with the i -th grid point given by a vector ξ_i in the xy -plane onto which the observables are projected. The desired quantitative assessment of the quality of the reconstruction could then be given in terms of a subsequent goodness-of-fit (GoF) evaluation, which would tell us how likely the reconstruction within this model is for the best set of parameters found before.

This idea is illustrated in the following using the cluster example from Sect. 5. We recall that the true 3-dimensional gravitational cluster potential $\varphi(R, Z)$ is observed under an angle of $i = 30^\circ$, and assume that we do not know the proper angle i in

advance. For setting up the χ^2 statistics we compute a series of single data and multiple data reconstructions with various values for the angles i and the weight factors. We then use Eq. 32 to evaluate the corresponding χ^2 function, and obtain a χ^2 value for every set of input parameters.

The minimum over all the χ^2 values then indicates the best choice for the inclination angle i and the weight factors. According to our qualitative analysis from Sect. 5 we would expect that the inclination angle i indeed should be very close to the true value.

Work on the quantitative estimation of the inclination angle and the weight factors α , β and γ using the approach sketched above is currently in progress. Preliminary results indicate that with the simulation data available in this study the main contribution to the χ^2 for a fixed inclination angle i does not result from the mismatch between reconstructed potential and true potential, but from discretization effects due to the finite grid. The question, if the above sketched determination of the inclination angle i and the weight factors α , β and γ is feasible for realistic observational data sets of finite sizes thus requires further investigation.

7. Discussion

With the advent of an ever increasing number of clusters, which have several superb data sets including lensing, X-ray and SZ-images, it is an interesting question whether it is possible to

obtain an improved reconstruction of the structure of individual clusters along the LOS by combining observational data from these different sources. In this paper we were able to devise an algorithm based on the Richardson-Lucy deconvolution algorithm that uses lensing, X-ray and Sunyaev-Zel'dovich data to gain information about the 3-dim. structure of a cluster of galaxies. The first implementation of this *multiple-data Richardson-Lucy* (MDRL) algorithm was applied to synthetic clusters generated in gas-dynamical simulations, and we found it to work stably and efficiently:

Starting from earlier work of Binney et al. (1990) on deprojection of elliptical galaxies from photometric data, an integral kernel for an axisymmetric cluster model was derived and integral expressions for the n -th projected distribution $\psi_n(x, y)$ and the n -th iterative estimate $\phi_n(R, Z)$ to the true potential $\phi(R, Z)$ were obtained, that are suitable for numerical evaluation. In particular, we found that the simple LOS integral for ψ_n is easier to evaluate and numerically more stable as the expression given in Binney et al. (1990), and thus is to be preferred.

It was shown that the three observables of interest, the lensing potential ψ , the X-ray luminosity S_x , and the Sunyaev-Zel'dovich temperature decrement ΔT_{SZ} can all be written as functionals of the gravitational potential $\phi(R, Z)$ assuming an appropriate equation of state. The lensing potential ψ by itself is given directly as a simple LOS integral over $\phi(R, Z)$, whereas S_x and ΔT_{SZ} both have an exponential dependence on $\phi(R, Z)$ mediated by the electron density within an isothermal hydrostatic intracluster gas model. S_x is here assumed to result in continuum bremsstrahlung of the gas distribution, and ΔT_{SZ} is due to Compton scattering of CMB photons passing through the hot cluster gas.

The practical implementation of the MDRL algorithm into a computer program led to a few important observations. The evaluation of the n -th iterative estimate $\phi_n(R, Z)$ requires integrations over ellipses on the projection plane, where the size and the relative location of the ellipse is determined by the current pair of (R, Z) values. In the X-ray and SZ case the logarithmic dependence on the projected quantities requires the use of cut-off criteria to minimize the magnification of small deviations between observed and reconstructed projected data.

A first application of the MDRL method to a cluster from gas-dynamical simulations showed that the approach already works well for single data reconstructions from ψ , S_x , or ΔT_{SZ} . The algorithm is very insensitive to the initial guess provided for ϕ ; qualitatively no significant difference in the reconstructed potentials obtained from a very simple constant value function or the realistic NFW model potential chosen as initial guesses were found. As expected theoretically, the X-ray and SZ reconstructions, which have their main contributions coming from the cluster core and are less affected by projection effects, give a better description of the core region, whereas the lensing potential that is only sensitive to the dark matter distribution, but more prone to projection effects, better reproduces the overall shape of the potential. Finally, we found that a combination of all three data sets within a multiple data reconstruction improves upon the single data results: the inner region is described as well as

in the X-ray and SZ case, and the description for larger (R, Z) radii lacking in the X-ray and SZ-case is compensated for by the lensing data.

We believe that this multiple data Richardson-Lucy reconstruction method will be a valuable and widely applicable tool.

Acknowledgements. We thank Matthias Bartelmann for suggesting this project and for many stimulating discussions. Klaus Dolag kindly provided the gas-dynamical simulation data. This work was supported by the ‘‘Sonderforschungsbereich 375-95 f ur Astro-Teilchenphysik’’ der Deutschen Forschungsgemeinschaft.

Appendix A: derivation of the kernel and formulation of the RL-scheme

The derivation of the kernel follows closely the derivation given in Binney et al. (1990) for the deprojection of elliptical galaxies. In order to derive the kernel $P(x, y|R, Z)$ we start with the following identity for ϕ ,

$$\phi(R, Z) = \int_0^\infty dR'^2 \int_{-\infty}^\infty dZ' \phi(R', Z') \delta(R^2 - R'^2) \delta(Z - Z'), \quad (\text{A.1})$$

which we insert into Eq. 5 for the LOS integral over ϕ and obtain

$$\psi(x, y) = \int_{-\infty}^\infty dz \int_0^\infty dR'^2 \delta[R^2(x, y, z) - R'^2] \times \int_{-\infty}^\infty dZ' \phi(R', Z') \delta[Z(x, y, z) - Z']. \quad (\text{A.2})$$

Next, we simplify $\delta(Z - Z')$ by substituting the coordinate transformation (4c) for Z and applying a computational rule for δ -functions². In this case we have

$$f(z_s) = y \sin i + z_s \cos i - Z' \stackrel{!}{=} 0 \Rightarrow z_s = \frac{Z' - y \sin i}{\cos i}, \quad (\text{A.3})$$

provided that $\cos i \neq 0$. Here and in the following we can restrict the discussion to the inclination angles in the range of $0 \leq |i| < \pi/2$, leading to non-zero, positive values for $\cos i$. Together with $f'(z) = \cos i$ and the corresponding substitution 3, 2.2 for $R(x, y, z)$ we arrive at

$$\psi(x, y) = \int_0^\infty dR'^2 \int_{-\infty}^\infty dZ' \int_{-\infty}^\infty dz \frac{\phi(R', Z')}{\cos i} \times \delta \left[x^2 + (y \cos i - z \cos i)^2 - R'^2 \right] \delta \left[z - \frac{Z' - y \sin i}{\cos i} \right]. \quad (\text{A.4})$$

Finally, integration of the second δ -function over z yields

$$\psi(x, y) = \pi \int_0^\infty dR'^2 \int_{-\infty}^\infty dZ' \phi(R', Z') \times \frac{\delta \left[(y \cos i - (Z' - y \sin i) \tan i)^2 - (R'^2 - x^2) \right]}{\pi \cos i}, \quad (\text{A.5})$$

² $\delta(f(x)) = \sum_s \frac{\delta(x - x_s)}{|f'(x_s)|}$, where $f' = \frac{df(x)}{dx}$. The function $f(x)$ is a real, differentiable function with $f(x_s) = 0$. The roots x_s are real and simple.

which is in the desired form of Eq. 6. We can identify the kernel

$$P(x, y|R, Z) = \frac{\delta[(\frac{y}{\cos i} - Z \tan i)^2 - (R^2 - x^2)]}{\pi \cos i}, \quad (\text{A.6})$$

and find that it is properly normalized:

$$\int_{-\infty}^{\infty} dx \int_{-\infty}^{\infty} dy P(x, y|R, Z) = 1. \quad (\text{A.7})$$

The second step 2b in the iterative RL-scheme reads in our case

$$\frac{\phi_{n+1}(R, Z)}{\phi_n(R, Z)} = \int dx \int dy \frac{\tilde{\psi}(x, y)}{\psi_n(x, y)} P(x, y|R, Z). \quad (\text{A.8})$$

For this second integral the evaluation of the probability kernel $P(x, y|R, Z)$ cannot be avoided. However, it is possible to eliminate the δ -function by again applying the same rule as before to $\delta(f(y))$ and by subsequently integrating over y .

For the quadratic equation

$$f(y) = \left(\frac{y}{\cos i} - Z \tan i\right)^2 - (R^2 - x^2) \stackrel{!}{=} 0 \quad (\text{A.9})$$

we find the two roots

$$y_{\pm} = \cos i \left(Z \tan i \pm (R^2 - x^2)^{1/2} \right), \quad (\text{A.10})$$

which for a fixed pair of cluster coordinates (R, Z) describe an ellipse in the observer's sky. Since

$$\begin{aligned} f'(y) &= \frac{2}{\cos i} \left(\frac{y}{\cos i} - Z \tan i \right) \\ \Rightarrow f'(y_{\pm}) &= \pm \frac{2}{\cos i} \sqrt{R^2 - x^2}, \end{aligned} \quad (\text{A.11})$$

we obtain after integration over y

$$\begin{aligned} \frac{\phi_{n+1}(R, Z)}{\phi_n(R, Z)} &= \\ \frac{1}{2\pi} \int dx \frac{1}{\sqrt{R^2 - x^2}} &\left[\frac{\tilde{\psi}(x, y_+)}{\psi_n(x, y_+)} + \frac{\tilde{\psi}(x, y_-)}{\psi_n(x, y_-)} \right]. \end{aligned} \quad (\text{A.12})$$

The integration over x in Eq. A.12 is limited to a finite range $[-R, +R]$. Thus it is convenient to introduce a new variable t via

$$\begin{aligned} x(t) = R \cos t &\Rightarrow x(-\pi) = -R \\ &\text{and } x(0) = R. \end{aligned} \quad (\text{A.13})$$

Utilizing that

$$\sqrt{R^2 - x^2} = R\sqrt{1 - \cos^2 t} = -R \sin t \quad \text{for } t \in [-\pi, 0], \quad (\text{A.14})$$

we arrive at our final result, namely a formulation for the second integral in the RL-scheme without δ -functions:

$$\begin{aligned} \frac{\phi_{n+1}(R, Z)}{\phi_n(R, Z)} &= \\ \frac{1}{2\pi} \sum_{\pm} \int_{-\pi}^0 dt &\frac{\tilde{\psi}(R \cos t, Z \sin i \pm R \sin t \cos i)}{\psi(R \cos t, Z \sin i \pm R \sin t \cos i)}. \end{aligned} \quad (\text{A.15})$$

References

- Bartelmann M., Steinmetz M., 1996, MNRAS 283, 431
 Bartelmann M., Narayan R., Seitz S., Schneider P., 1996, ApJ 464, L115
 Binney J.J., Davies R.L., Illingworth G.D., 1990, ApJ 361, 78
 Böhringer H., Schwarz R.A., Briel U.G., 1993, In: Chincarini G., Iovino A., Maccacaro D. (eds.) *Observational Cosmology*. Astron. Soc. of the Pacific Conference Series
 Cavaliere A., Danese L., DeZotti G., 1979, A&A 75, 322
 Clowe D., Luppino G., Kaiser N., Gioia I., 2000, ApJ 539, 540
 Dehnen W., Gerhard O., 1993, MNRAS 261, 311
 Dehnen W., Gerhard O., 1994, MNRAS 268, 1019
 Dolag K., Bartelmann M., Lesch H., 1999, A&A 349, 351
 Gunn J.E., 1978, In: Maeder A., Martinet L., Tammann G. (eds.) *Observational Cosmology 1*, Geneva Obs., Sauverny, p. 3
 Lucy L.B., 1974, AJ 79, 745
 Lucy L.B., 1994, A&A 289, 983
 Merritt D., 1987, ApJ 313, 121
 Navarro J.F., Frenk C.S., White S.D.M., 1996, ApJ 462, 563
 Navarro J.F., Frenk C.S., White S.D.M., 1997, ApJ 490, 493
 Richardson W., 1972, J. Opt. Soc. Am. 62, 55
 Rybicki G., Lightman A., 1979, *Radiative processes in Astrophysics*. John Wiley & Sons
 Schneider P., Ehlers J., Falco E.E., 1992, *Gravitational Lenses*. Springer-Verlag
 Schneider P., Seitz C., 1995, A&A 294, 411
 Shu F.H., 1991, *The Physics of Astrophysics*. Vol. 1 and 2, University Science Books
 Silk J., White S., 1978, ApJ 226 L103
 Sulkanen M.E., 1999, ApJ 522, 59
 Sunyaev R., Zel'dovich Y., 1972, *Comments Astrophys. Space Phys.* 4, 173
 Sunyaev R., Zel'dovich Y., 1978, *Comments Astrophys. Space Phys.* 2, 66
 Sunyaev R., Zel'dovich Y., 1980, ARA&A 18, 537
 The L.S., White S., 1986, AJ 92, 1248
 White S., Frenk C., 1991, ApJ 379, 52